ELSEVIER

Ground deformation patterns at Mt. Etna from 1993 to 2000 from joint use of InSAR and GPS techniques

M. Palano [a,*], G. Puglisi [a], S. Gresta [b]

[a] *Istituto Nazionale di Geofisica e Vulcanologia, sezione di Catania, P.zza Roma, 2, 95123 Catania, Italy*
[b] *Università degli Studi di Catania, Dipartimento di Scienze Geologiche, Corso Italia 57, 95129 Catania, Italy*

Abstract

Combined GPS measurements and radar interferometry (InSAR) have been applied at Mt. Etna to study the ground deformation affecting the volcano both over the long- (1993–2000) and short-term (1997–1998 and 1998–2000). The aim was to better understand the dynamics of the volcano during the magma-recharging phase following the 1991–93 eruption.

Since 1993, InSAR and GPS data indicate that Mt. Etna has undergone an inflation. A deep intrusion was detected by InSAR, on the western flank of the volcano, between March and May 1997. In the following months, this intrusion rose up leading to a seismic swarm occurring in January 1998 in the western sector. This now shallow intrusion is confirmed by GPS data. From 1998 to 2000, a general deflation affecting the upper part of the volcano was detected.

Over the whole study period, a continuous eastward to south-eastward motion of the eastern sector of the volcano was also evidenced. The analytical inversions of GPS data inferred a plane dipping about 12°ESE, located beneath the eastern flank of the volcano at a depth of 1.4 km b.s.l. The movement along this plane is able to reproduce the observed south-eastward motion of a sector bounded northward by the Pernicana fault, westward by the North–East Rift and the South Rift, and southward by the Mascalucia–Tremestieri–Trecastagni fault system. InSAR data have validated this model.
© 2007 Elsevier B.V. All rights reserved.

1. Introduction

GPS is the most suitable technique to measure ground deformations. However, it provides spot data, *i.e.* they refer to network vertices whose number rarely exceeds the order of tens in areas of hundreds, often thousands, of square kilometres. InSAR allows acquiring data continuously on the surface and thus, even if with a lower absolute accuracy than GPS, its introduction has been seen as the only way to continuously map the gradients of ground deformation patterns. Hence an approach that integrates InSAR–GPS results has the potential to investigate highly accurate deformations (*i.e.* at subcentimetre levels) with unprecedented spatial coverage.

In this paper, an integrated InSAR–GPS approach will be applied in order to better constrain both long- and short-term ground deformation patterns affecting Mt. Etna volcano during 1993–2000. Here, preliminary results published by Palano et al. (2007) are expanded. Since GPS measurements are usually more accurate

---

than InSAR, they are assumed more informative than InSAR data, at least near the benchmarks. Thus in a first step, GPS data were inverted adopting classical formalisms (Mogi, 1958; Okada, 1985). Then, the surface deformation pattern obtained from this first model was used to compute a synthetic interferogram, which was compared to the experimental InSAR data. Finally, through a trial-and-error approach an acceptable model that jointly fits both GPS and SAR datasets was obtained.

We will show that ground deformations due to magma movements within the plumbing system of the volcano (magmatic sources) and ground deformation due to activity of several faults that dissect the volcano edifice (tectonic sources) are both detectable with our approach.

2. Geological and volcanological setting

Mt. Etna is a Quaternary polygenetic volcano located on the east coast of Sicily. It stands between two first-order tectonic elements: the Apenninic–Maghrebian Chain to the north, and the Hyblean Foreland to the south (Fig. 1).

To the east, two major structural lineaments separate the continental lithosphere of eastern Sicily from the oceanic lithosphere of the Ionian basin (Lentini, 1982): the former can be traced northwards along the NE-SW striking Messina fault system to the inner side of the Calabrian orogenic arc, while the latter can be traced southwards along the NNW-SSE-oriented Malta Escarpment to the Hyblean Foreland (Monaco et al., 1997).

The northern and western parts of the volcano edifice overlie and are buttressed over a pre-existing topography developed in metamorphic and sedimentary rocks belonging to the southward verging system of thrusted nappes of the Apenninic–Maghrebian Chain. The southern and eastern flanks of the edifice, instead, overlie marine plastic clays of Quaternary age, which are accumulated in the foredeep created on the tectonically depressed northern margin of the northward-dipping downgoing Hyblean Foreland (Lentini, 1982).

The Pernicana fault system, on the north-eastern flank, and the Mascalucia–Tremestieri–Trecastagni fault system, on the southern flank, represent two of the most important features for understanding the dynamics of the volcano (Lo Giudice et al., 1982). These faults are connected through the North–East Rift (hereafter NE Rift) and South Rift, crossing the summit craters to define a large unstable sector (Fig. 1). This sector of the volcano is affected by a long-term sliding toward ESE, resulting from the interaction between

gravity, thermal effects, regional tectonics and dyke intrusions (McGuire and Pullen, 1989; Borgia et al., 1992; McGuire et al., 1996; Rasà et al., 1996; Borgia et al., 2000; Froger et al., 2001) along a poorly constrained basal detachment (Lo Giudice et al., 1982; Bonforte and Puglisi, 2003; Lundgren et al., 2003).

The Pernicana fault (Fig. 1), representing the northern boundary of this sector, can be traced for about 8 km, with an approximate east–west strike. Displacement varies from almost pure down-to-the-south dip-slip at its upslope end, through left-oblique slip in its middle reaches, to almost pure left-lateral strike-slip at its eastern end (Azzaro et al., 2001). Westwards, it joins with the NE Rift, which represents one of the most active sectors of the volcano (Rasà et al., 1996) and could be considered the northern half of the western boundary of the sliding sector.

The southern half of the western boundary of the sector is represented by the South Rift (Rasà et al., 1996) joining, south-eastward, with the Mascalucia–Tremestieri–Trecastagni fault system (Fig. 1). This fault system is made up of a number of NNW-SSE striking faults displaying prominent linear scarps. The fault zone shows evident right-lateral displacement and is also characterised by very shallow seismicity, with focal depths typically of 1–2 km. It has been interpreted as the southern boundary of the sliding sector (Rasà et al., 1996). However, other authors identify the Ragalna fault (Fig. 1) as the south-western boundary of the sliding sector (Borgia et al., 1992; Rust and Neri, 1996). The Ragalna fault displays a consistent pattern of right-oblique displacement of cultural features as well as open left-stepping en echelon fissures. Focal mechanism solutions of local shallow earthquakes show right-lateral slip (Azzaro, 1999). The activity of this fault has also been recently highlighted by InSAR data (Lundgren et al., 2004).

Several other faults dissect the eastern sector of the volcano (Fig. 1), all recognized by significant shallow seismicity ($h < 5$ km) and/or creep phenomena (Gresta et al., 1997).

After the end of the 1991–93 eruption, a period of low volcanic activity (Fig. 2a), characterised by a continuous degassing interrupted only by a few phreatic explosions, began at the summit craters (Coltelli et al., 1998). Magmatic activity resumed in July 1995, at the Bocca Nuova crater (BNC) then spread alternately to the other craters in the following months (Coltelli et al., 1998) (Fig. 2a). In January 1998, a seismic swarm ($M_{max} = 3.7$) marked a shallow dike intrusion below the summit area (Bonaccorso and Patanè, 2001). In the following months, an increase in eruptive activity,
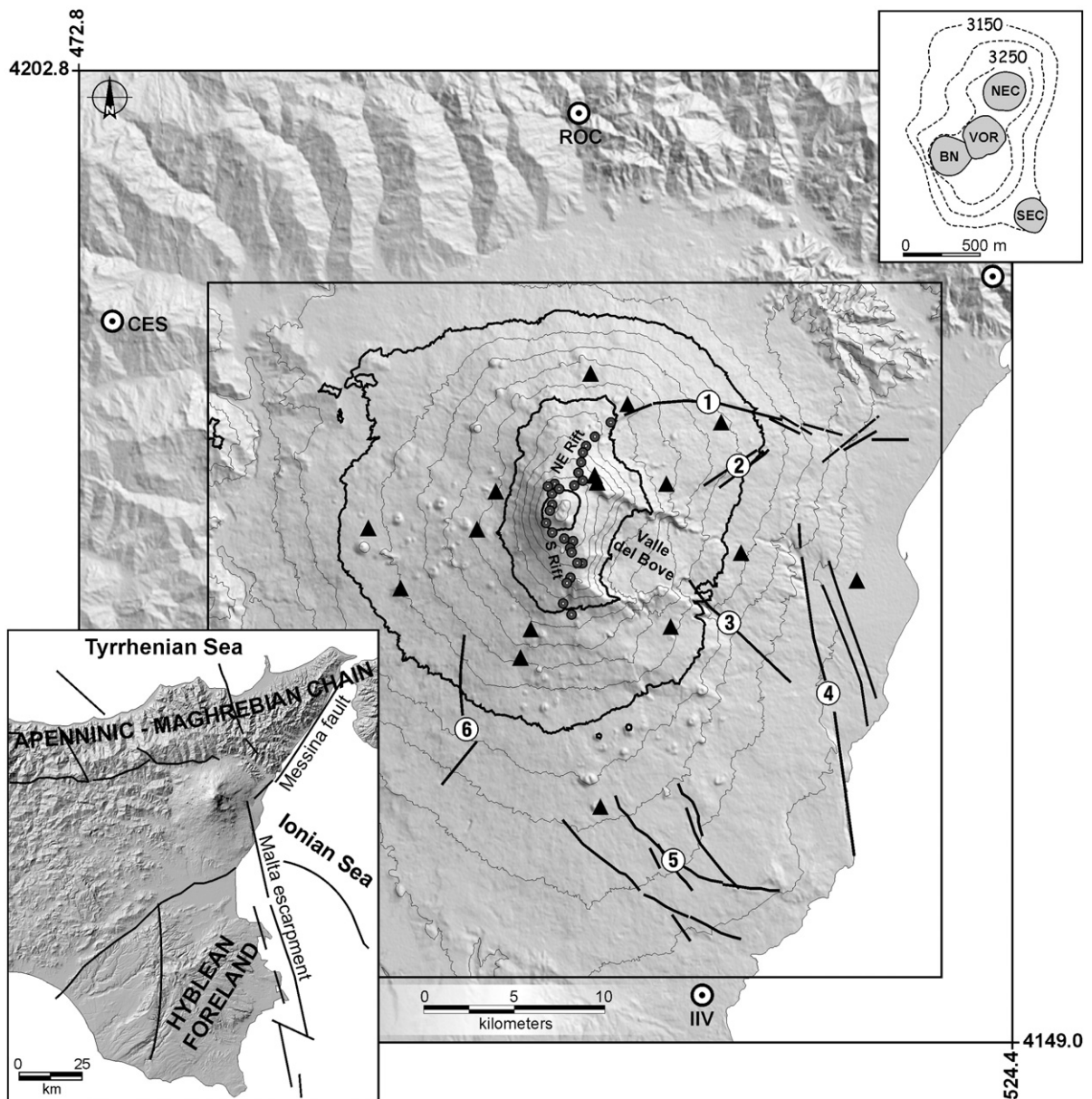
Fig. 1. Sketch map of Mt. Etna: (1) Pernicana fault; (2) Ripe della Naca fault; (3) Santa Venerina fault; (4) Timpe fault system and Moscarello fault; (5) Mascalucia–Tremestieri–Trecastagni faults system; (6) Ragalna fault. Mt. Etna GPS network is also reported: white circles for external reference benchmarks, black triangles for inner benchmarks and dark grey points for N–S kinematic profile (see text for details). The box indicates the area shown in Figs. 3, 4, 5 and 6. The upper inset reports the four central craters of Mt. Etna's summit area: BN, Bocca Nuova; NEC Northeast Crater; SEC, Southeast Crater; VOR, Voragine. In the lower inset, a simplified structural map of eastern Sicily is also reported. Coordinates are in UTM projection, zone 33N.

characterised both by strombolian and effusive activities, was observed. At the end of 2000 and during the first weeks of 2001, Mt. Etna was quiet. A new flank eruption started on the southern flank in July 2001 (INGV staff, 2001). A detailed chronogram of the activity at the four Mt. Etna craters is reported in Fig. 2a.

3. Ground deformation from GPS data

Routine use of GPS for monitoring ground deformations started at Mt. Etna in 1988, when a network of 18 benchmarks was surveyed by both GPS and EDM techniques (Briole et al., 1992). Since then, the network
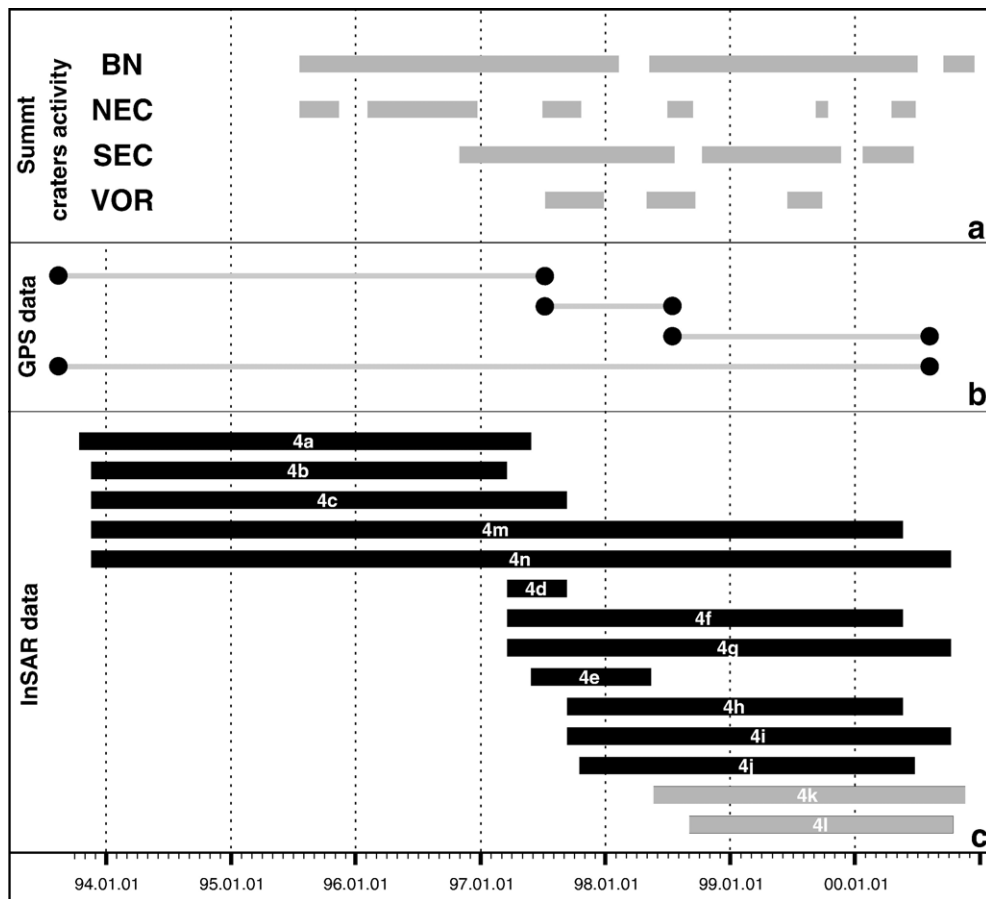
Fig. 2. (a) Graphic illustration of the activity at the summit craters during 1993–2000; (b) time coverage for the GPS data; (c) time coverage for InSAR data (black bars for ascending passes and gray bars for descending passes).

has been improved and surveyed by GPS almost yearly. The surveys are usually performed in static mode, but a kinematic profile crossing the summit area, from south to north, was also included in the network since the 1996 survey. During static surveys receivers are installed for 4–6 hours on the benchmarks, while the kinematic surveys are carried out by covering the profile in "fore and back" mode, by occupying each benchmark for 3–5 minutes (details for kinematic surveys are in Puglisi and Guglielmino, 1995).

In this paper, data collected from GPS surveys, between 1993 and 2000 were analysed in order to investigate both long- and short-term ground deformation patterns. In particular, in order to allow the integration between GPS and InSAR results, comparisons among the 1993, 1997, 1998 and 2000 surveys were analysed (Fig. 2b). While here we refer to the Puglisi et al. (2001) solution for the 1993 survey, the other three surveys were re-processed (1997 and 1998

surveys) or processed for the first time (2000 survey) in this paper.

Data from each survey were processed using the Trimble Geomatics Office software, version 1.5. International GPS Service (IGS) antenna calibration models were introduced to avoid biases deriving from the different electromagnetic characteristics of the antenna models used during the surveys. Precise ephemeredes produced by the IGS were also introduced into the processing, in order to achieve higher accuracy during the baselines computation (Beutler et al., 1990). The data were processed using both GPS frequencies L1 and L2. In particular, their combination L3, the ionosphere-free observable, was used for baselines longer than 10 km to eliminate the ionospheric effects. The use of L3 observable always introduces a noise that becomes stronger than the ionospheric effect for short distances, so only the L1 frequency was used to process baselines shorter than 10 km. The baseline solutions

resulting from each survey processing were then adjusted. Each adjustment was performed in two steps. The whole set of baseline solutions was initially adjusted according to the hypothesis of the inner constraints (in practice the network has been fixed to its centroid); this step allows the consistency of the data to be validated. Then the network was fixed assuming an appropriate set of coordinates for the reference frame. Each survey was fixed to the coordinates of IIV, CES and ROC benchmarks (Fig. 1) resulting from the final solution of the survey carried out a few days before the 2001 eruption (Palano, 2003).

As a final step, the horizontal and vertical displacements of each benchmark were estimated: (i) by comparing the results of the adjustment for the 1997–1998 and 1998–2000 comparisons, and (ii) by combining different subsequent solutions for the 1993–1997 and 1993–2000 comparisons (for the 1993 survey, as already mentioned, we referred to the Puglisi et al., 2001 solution).

The results of the comparisons are reported in terms of horizontal displacement vectors and vertical motions of each GPS benchmark (Fig. 3). The calculated uncertainty is typically 0.3–0.4 cm in the horizontal components and about 0.7–1.1 cm in the vertical component. For the N–S kinematic profile, the uncertainty is typically 0.6–0.8 cm in the horizontal components and 1.3–1.6 cm in the vertical component.

The displacement vectors calculated by GPS measurements for the September 1993–July 1997 comparison are reported in Fig. 3a. The horizontal displacements show a general radial pattern with respect to a centre of deformation located on the upper western flank. The eastern and south-eastern sectors are indeed affected by a strong horizontal eastward displacement, with respect to the western and summit sectors. The horizontal deformation ranges from 2 to 12 cm. Concerning the vertical displacement, there was a general uplift of the whole edifice with a maximum of 8 cm located on the northern part of the summit area.

The ground deformations, occurring during the July 1997–July 1998 time interval, are reported in Fig. 3b. From this comparison, information from the N–S kinematic profile provides a very dense sampling of the deformation of the upper part of the volcano (Fig. 3e). The vertical displacements measured at the network's benchmarks show a general uplift of the whole edifice. The largest vertical displacement was detected along the N–S kinematic profile, ranging from 3 cm to 9 cm. An uplift of about 3–4 cm was also measured on the western flank of the volcano, while a subsidence of about 4 cm affected the eastern side. The

horizontal displacements again show a different behaviour between the eastern and western flanks of the volcano. The western sector is indeed affected by a strong horizontal component of motion, with a clearly south-westward direction of deformation. The same direction is shown by the central-southern part of the N–S kinematic profile. The eastern flank shows a lesser motion (about 1–2 cm), trending ESE in the northern part and to S in the southern part. The horizontal deformation ranges from 0.5 cm to 5 cm.

Between July 1998 and July 2000, the volcano edifice was affected by a marked subsidence, up to − 10 cm on the summit and NE Rift areas (Fig. 3c, f). The directions of the horizontal displacements observed at the benchmarks indicate that the volcano is generally expanding mainly to the SE–S and W. The horizontal component of deformation ranges from 0.6 cm to 5 cm.

In Fig. 3d, the displacement vectors calculated by GPS measurements for September 1993–July 2000 comparison are reported. The horizontal displacements show a general radial pattern of the motion, with respect to a centre of deformation located on the upper western flank, as just observed for the 1993–1997 period. The amplitude of the horizontal deformations ranges from 5 to 16 cm. Regarding the vertical displacement, a general uplift of the whole edifice with a maximum of 10 cm located on the upper southern flank is observed.

4. Ground deformation from InSAR data

The radar images over Mt. Etna are taken by the ERS1/2 satellites. The selection of the images was performed by inspecting the ERS archives with the DESCW software, available at the Eurimage web site.

The following two criteria have been adopted for choosing the images: (i) to obtain image pairs having the minimum perpendicular baseline component available (to minimize temporal decorrelation) and (ii) to obtain orbit pairs in order to study the same period investigated by GPS techniques (Fig. 2c).

Table 1 lists the interferometric orbit pairs of data. They are acquired during both ascending (frame 747) and descending passes (frame 2853). The satellites travel from about S10°E to N10°W for the ascending passes and the SAR sensor is directed ∼ N80°E. In descending passes, the satellites travel from about N10°E to N10°W and the SAR sensor is directed ∼ N80°W. The procedure used for the generation of interferometric products relevant to the selected image pairs is called two-pass interferometry (Massonnet and Feigl, 1998). This approach seeks to exploit all the external information available for a site, in particular the
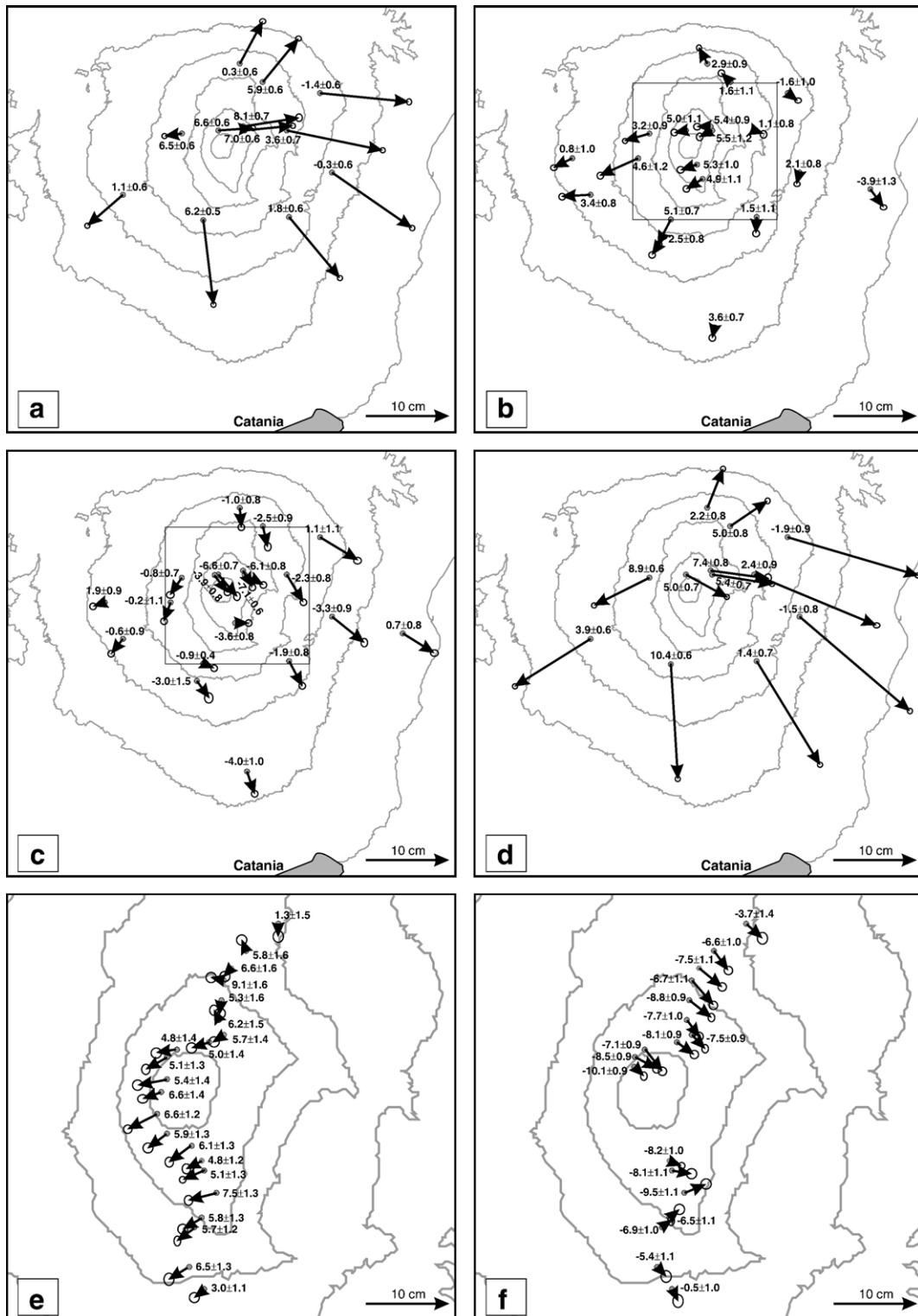
Fig. 3. Displacement vectors and height variations on Mt. Etna volcano: (a) from 1993 to 1997; (b) from 1997 to 1998; (c) from 1998 to 2000; (d) from 1993 to 2000; (e) zoom on the NS profile along the summit area for the 1997–1998 time interval and (f) zoom on the NS profile along the summit area for the 1998–2000 time interval. The uncertainty in the vertical component is about 0.7–1.1 cm; for the benchmarks belonging to the NS profile, the uncertainty in the vertical component is about 1.3–1.6 cm. Elevation contour interval is 0.5 km.

Table 1
InSAR image pairs formed and relevant parameters. "⊥ B" is the magnitude of the perpendicular baseline orbit separation of the InSAR pair. "ha" is the "altitude of ambiguity"; this is the ground altitude difference that generates one fringe in an interferogram. The higher the altitude of ambiguity, the fewer the residual topographic fringes in the interferogram (Massonnet and Feigl, 1998)

| Image pair	Frame	Time Span (days)	⊥ B (m)	ha (m)	Figure
1993.10.17–1997.05.28	747	1319	19	485	4a
1993.11.21–1997.03.19	747	1214	− 80	115	4b
1993.11.21–1997.09.10	747	1389	− 2	4606	4c
1993.11.21–2000.05.17	747	2369	− 66	139	4m
1993.11.21–2000.10.04	747	2509	− 40	230	4n
1997.03.19–1997.09.10	747	175	78	118	4d
1997.03.19–2000.05.17	747	1155	14	658	4f
1997.03.19–2000.10.04	747	1295	40	230	4g
1997.05.28–1998.05.13	747	350	− 80	115	4e
1997.09.10–2000.05.17	747	980	− 64	144	4h
1997.09.10–2000.10.04	747	1120	− 38	242	4i
1997.10.15–2000.06.21	747	980	56	164	4j
1998.05.20–2000.11.15	2853	910	10	921	4k
1998.09.02–2000.10.11	2853	770	20	460	4l

topography, through a Digital Elevation Model (DEM). As source of the topographic information, a photogrammetric DEM, with a measured accuracy of 10 m has been considered. The orbital parameters of each pair were refined by a more accurate estimate of the state vector positions as calculated by DEOS (Delft orbits). After removing all fringes related to ground elevation, only the fringes representing surface displacements remain. In the interferogram, each fringe is directly related to the radar wavelength and represents a displacement relative to the satellite of half wavelength (2.83 cm for ERS satellites).

Fig. 4 shows the interferograms listed in Table 1. These images represent maps of deformation from 1993 to 2000 along the radar Line Of Sight (LOS), and lead to the following qualitative observations in time and space, useful to perform the successive quantitative analysis of GPS and InSAR results:

1. A first visual inspection of the interferograms is a good approach to evaluate their quality. By adequately combining the interferograms that cover identical time intervals, it is possible to evaluate the internal consistency of the dataset here considered. The possible combinations are: 4c should be the sum of 4b and 4d; 4m should be the sum of 4b and 4f (or the sum of 4c and 4h); 4n should be the sum of 4b and 4g (or the sum of 4c and 4i); 4f should be the sum of 4d and 4h; 4g should be the sum of 4d and 4i. This inspection confirms that the observed ground deformation patterns shown by these interferograms have a good internal consistency. The interferograms whose consistency with the others cannot be inspected are 4a, 4e, 4j, 4k and 4l. Those interferograms should be considered with caution in the following analysis.

2. We compared pairs of interferograms with short-time delay from each other (4a–4c, 4m–4n, 4f–4g) on the westernmost parts of the volcano. We selected this area because ground deformations (mainly the vertical components) are usually less intense than in other sectors of the volcano. This kind of analysis should provide an estimate of the errors due both to atmospheric and/or other secondary perturbing effects. The discrepancies in the pairs of interferograms range from 1/4 to 1/3 of half wavelength (0.7 to 0.9 cm), but these values seem smaller compared with the tropospheric effects indicated either by modelling approach (*e.g.* Delacourt et al., 1998; Beauducel et al., 2000) or by direct measurements by Bonforte et al. (2001). Thus we suspect that the images used to produce each interferogram analysed above could contain atmospheric effects which compensated each other. Based on this evidence, in the following, these interferograms will be used only to reinforce conclusions achieved independently (*e.g.* by using other interferograms and/or GPS-based models), because any deformation model based only on these interferograms could be biased by "undetectable" atmospheric artefacts.

3. The interferograms reported in Fig. 4 allow the investigation of five different time intervals: from 1993 to 1997 (Fig. 4a, b, c), from 1997 to 1998 (Fig. 4d, e), from 1997 to 2000 (Fig. 4f, g, h, i, j), from 1998 to 2000 (Fig. 4k, l) and from 1993 to 2000 (Fig. 4m, n).

   a. From 1993 to 1997, the deformation patterns show a general LOS shortening, although the
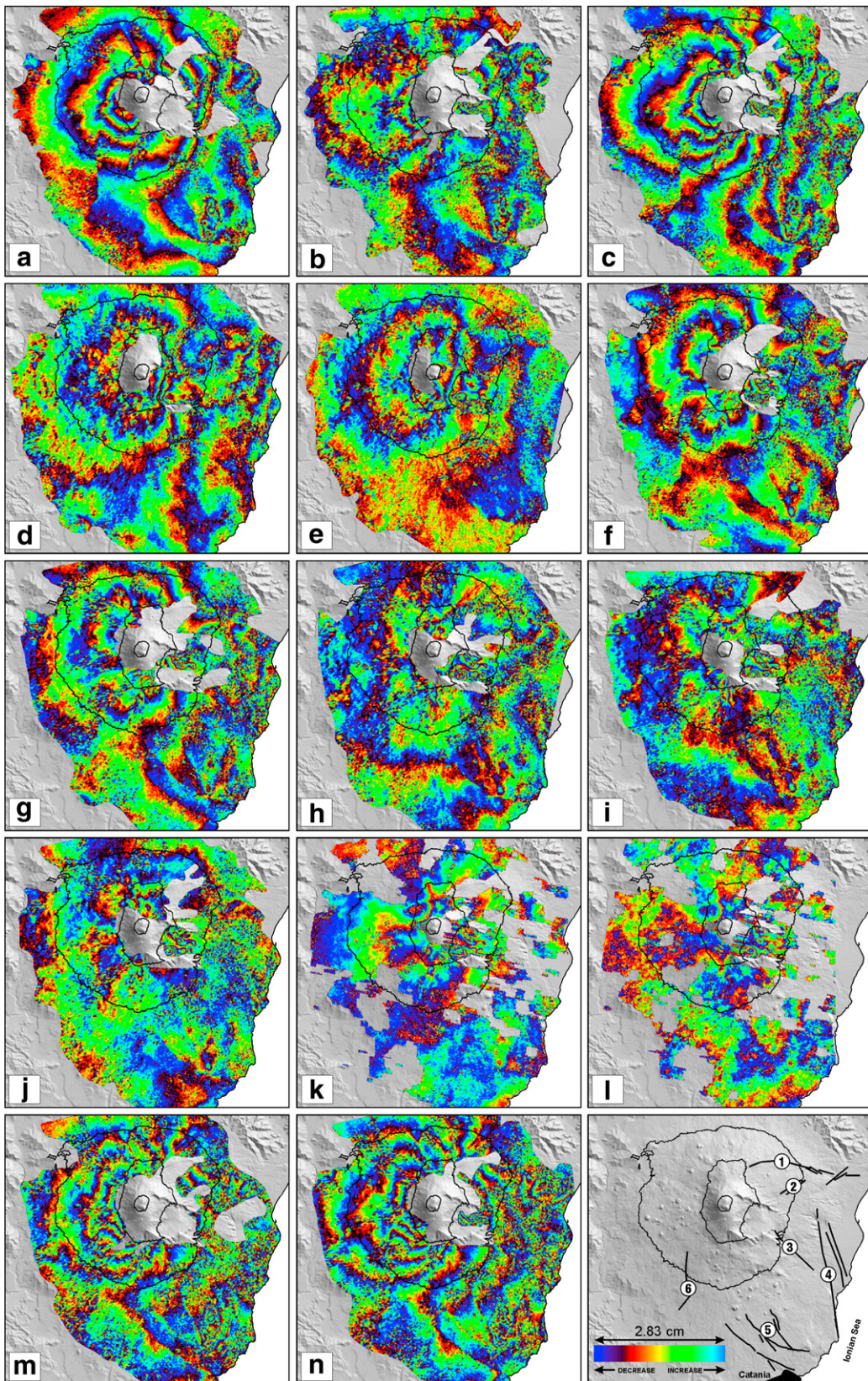
comparison between 4a, 4b and 4c interferograms suggest that the shortening rate was not constant throughout this interval. The 4b and 4c interferograms, indeed, show different patterns even if they cover similar time spans; in particular, 4b interferogram measures smaller deformation than the 4c one. Considering that both interferograms began in November 1993 but end in March and September 1997 respectively, it is evident that some "changes" occurred from March to September 1997. This first conclusion confirms the analysis of Bonforte et al. (2001), who measured about 1.5–2 fringes from the base of the volcano up to the summit, from March to September 1997, after filtering the atmospheric effects. Furthermore, because 4a and 4c interferograms have a similar deformation pattern, even if they did not begin and end at the same time, it appears that the increase in the uplift rate occurred in the March–May 1997 time interval (the only period not in common between the two 4a and 4b interferograms and included in 4c). The shape of the uplift, from 4a and 4c interferograms, suggests that the source was relatively deep, owing to the large affected area. However, the suspicion of atmospheric effects on both 4a and 4c interferograms (see point 2) suggests that this last conclusion should be reinforced by further independent analysis.

b. The 4d and 4e interferograms, relevant to 1997–1998 time interval, show similar deformation patterns with a marked uplift centred slightly westward with respect to the summit craters and roughly elliptically shaped, with elongation trending NNE-SSW. The 4d interferogram shows a larger deformed area with respect to the 4e one, interpreted as the effect of a deep source. The evidence of a deep source is lost in the 4e interferogram, whereas fringes close to the summit area here evidence a shallow source. This confirms the activation of a deep source between March and May 1997, as suggested in point 3a, and constrains the presence of a shallow source between May 1997 and May 1998.

c. The analysis of the 1997–2000 time interval allows the ground deformation events detected between March 1997 and May 1998 to be better

constrained. The interferograms 4f and 4g show a general LOS uplift, whereas no significant ground deformation patterns are recognizable in 4h, 4i and 4j interferograms. This analysis reinforces the evidence that the deep and shallow sources were active between May 1997 and September 1997.

d. In the 4k and 4l interferograms, relevant to 1998–2000 time interval, more than one fringe can be recognized, suggesting a deflation of about 5–6 cm of the volcano. Although large parts of these interferograms have very low coherency values, the deflated area seems to include the summit area and the highest western and northern flanks of the volcano.

e. The 4m and 4n interferograms span the 1993–2000 period. The ground deformation pattern measured has a similar shape to that observed for the 1993–1997 period, but it presents a higher number of concentric fringes, as expected due to the longer time span covered. In this case too, the fringes are centred on the upper western flank of the volcano edifice, accounting for more than 14 cm of uplift in the LOS satellite direction.

4. In many interferograms (Fig. 4a, b, c, e, f, g, h, i, j, m, n), three elongated phase discontinuities are visible, between the southern flank of Mt. Etna and the coast. They are located in the area of Mascalucia–Tremestieri–Trecastagni fault system. Two of them are curved with a northeast concavity, while the other one is slightly curved with a southwest concavity. All these have a sharp increase in phase to the northeast, which can be interpreted as a moving away from the northeastern area with respect to the south-western area.

5. The 4a, 4c, 4f, 4m and 4n interferograms show another elongated north–south phase discontinuity located in the area of the Ragalna fault, fitting this feature very well (Fig. 4) (Froger et al., 2001). The phase discontinuity corresponds to an eastward increase of the phase, i.e. an eastward lowering. This motion is compatible with the general (normal and dextral) motion identified on the Ragalna fault (Rust and Neri, 1996).

6. Another phase discontinuity located on the eastern flank of the volcano, NNW-SSE trending, is shown in the 4a, 4b, and 4m interferograms (Fig. 4). This fringe feature spatially fits well a tectonic lineament

Fig. 4. Example of interferograms showing deformation of Mt. Etna volcano for various time periods between 1993 and 2000: (a) 93.10.17–97.05.28; (b) 93.11.21–97.03.19; (c) 93.11.21–97.09.10; (d) 97.03.19–97.09.10; (e) 97.05.28–98.05.13; (f) 97.03.19–00.05.17; (g) 97.03.19–00.10.04; (h) 97.09.10–00.05.17; (i) 97.09.10–00.10.04; (j) 97.10.15–00.06.21; (k) 98.05.20–00.11.15; (l) 98.09.02–00.10.11; (m) 93.11.21–00.05.17; n) 93.11.21–00.10.04. Each fringe represents a change in phase corresponding to 2.83 cm of LOS. We use the convention that positive motion is toward the satellite. Areas that lack interferometric coherence are uncoloured. Additional information on SAR images used for the interferograms are given in Table 1. In the lower right corner a sketch map of Mt. Etna showing the main tectonic features recognized in interferograms (see text in Section 4 and Fig. 1 for details) is also reported.

known as Moscarello fault. The phase discontinuity corresponds to an eastward increase of the phase, *i.e.* an eastward subsidence, in good agreement with the normal motion already identified on the Moscarello fault (Monaco et al., 1997).

7. The Pernicana fault motion has not been resolved by InSAR; however, some phase discontinuities are clearly visible on the upper part of the eastern flank, abruptly interrupted on the same area of Pernicana fault; they are not visible to the north of this structure (Fig. 4a, c, e, m, n).

8. Localized fringes are also visible in Valle del Bove area (Fig. 1) showing a local subsidence, well correlated with the 1986–87, 1989 and 1991–93 lava fields. This subsidence can be interpreted as a combination of a lava field compaction, still considerable several years after the eruptions, and of a viscoelastic relaxation of the surrounding material, as Briole et al. (1997) suggested. Moreover, some additional subsidence effects can also be easily detected north of Catania (Fig. 4a, b, c, f, g, h, i, j, m, n), which are probably induced by pumping operations at water wells.

5. Model inversions

In order to model the observed displacement, the surface deformation can be estimated assuming simple dislocations (Okada, 1985) and/or point sources of pressure change (Mogi, 1958).

The inversion of ground deformation data is a process aimed at determining the parameters of a specific ground deformation source model from the data collected in the field. It can be performed by using analytical (generalised least-square) or numerical (neural networks, simplex, simulated annealing). In any case, these strategies are normally adopted to invert a relatively low number of geodetic data. The introduction of InSAR data changes not only the number of data to be inverted, but also the quality of data. Indeed, they are mono-dimensional and their quality varies widely across the interferogram. These facts severely reduce, or in some cases prevent, the possibility of using the least-square (L.S.) approach conventionally adopted to invert geodetic data.

Therefore, in order to interpret the observed ground deformations, the methodology here used is the following:

1. Inversions of ground deformation detected by GPS data adopting the Mogi and/or Okada formalisms by using L.S. or simple numerical approaches. In this step, both horizontal and vertical GPS components were inverted by taking into account the experimental errors.

2. Computation of the three-component vectors at each point of a grid covering the entire volcano for each modelled source of deformation and projection of the expected ground deformation along the LOS of each interferogram. In this step the fringes calculated from the model were compared with those observed in order to obtain the residual interferograms (the difference between modelled and observed interferograms).

3. Refinement of the source parameters by using a trial-and-error approach in order to obtain an acceptable model that jointly fits both GPS and InSAR data.

This approach constrains the models even though some areas, like the north-western part of the volcano edifice, lack GPS stations.

5.1. Inversion of the ground deformation measured from 1993 to 1997

The ground deformation pattern affecting Mt. Etna volcano during this time interval has been inverted in order to find the source producing the observed deformation.

Looking at the particular shape of the height variation and the radial pattern of the horizontal displacement vectors, a preliminary inversion of the GPS dataset by using the Simplex algorithm (Nunnari et al., 1995; Puglisi et al., 2001) was performed adopting a pressure source model (Mogi, 1958). The parameter space has been sampled by running about 350 minimum function searches, each search starting from a different set of parameter values. Starting points were arranged on a 10 km spaced grid centred beneath the summit craters area; for each horizontal position, four different depths (1, 3, 5 and 8 km) were given, and for each depth, two different strength values (McTigue, 1987) were assumed ($2 * 10^8$ and $5 * 10^8$ Pa m^3). Values of 30 GPa and 0.25 were assumed in the inversion for the shear modulus and Poisson's ratio respectively. The rigidity chosen corresponds to a typical value of crustal rigidity commonly used in modelling works (*e.g.* Williams and Wadge, 2000; Trasatti et al., 2003) which is found to be an average rigidity value for Mt. Etna (Chiarabba et al., 2000). All the solutions of the searches converged to a unique pressure source located beneath the upper western flank of the volcano, at a depth of 6.8 km b.s.l., with a strength of $4.17 * 10^{17}$ Pa m^3. Nevertheless, this model cannot explain the whole observed ground deformation on the eastern flank of

the volcano. This partial disagreement highlights a more complex dynamics than the one predicted by a pressure source alone. For this reason, a further inversion by using an L.S. approach was performed, starting from the results of the last one and introducing into the computation a sub-horizontal source (hereafter "plane of sliding"), lying beneath the eastern flank, previously defined by inverting GPS data acquired during the 1994 and 1995 surveys (Bonforte and Puglisi, 2003) and furthermore refined by using a larger GPS dataset (Palano, 2003).

Then, for the 1993–1997 inversion, the positions and dimensions of the sub-horizontal structure were kept fixed to those found by the last step, inverting only its dip- and strike-motion (its opening was forced to zero). The results of this last inversion enhanced the reliability of the calculated displacements. On the western flank, they remained close to the observed ones as in the previous data inversion, whereas on the eastern flank, the calculated horizontal displacements rotated and fitted more closely with the observed ones. Then, the synthetic interferogram (in ascending mode) for the sources modelled from GPS data was calculated. The residual interferograms show a misfit both on the eastern and western flanks. Then, we fine-tuned the pressure source parameters in order to produce a simulated interferogram that best matched the observed one (Fig. 4a, c) at least on the western flank of Mt. Etna. On the eastern flank, indeed, the synthetic deformation pattern produced by a simple dislocation source cannot reproduce the actual deformation pattern measured by InSAR. The final results of this inversion are summarized in Tables 2a and 3. The predicted vector displacements, the synthetic and residual interferograms are reported respectively in Figs. 5a and 6a, b, c.

5.2. Inversion of the ground deformation measured from 1997 to 1998

Between 1997 and 1998, a general uplift of the whole volcano edifice is evident (Fig. 3b). The orientation of the horizontal displacement vectors suggest that ground deformation data might be used to constrain the inversion of a dislocation model rather than a pressure source.

The same GPS dataset was previously processed using both different processing software and different sets of coordinates for the reference system. The ground deformation pattern resulting from the comparison has a similar shape and only a substantial difference regarding the height change is noteworthy (Puglisi and Bonforte, 2004). Three sources were detected: a dyke located on

the north-western flank of the volcano at 0.7 km a.s.l. and two sliding surfaces located under the southern and eastern flanks, respectively at depths of 0.5 km a.s.l. and 1.7 km b.s.l. (Puglisi and Bonforte, 2004). This period also provides an opportunity to compare the GPS-measured ground deformation pattern with the effects of a shallow intrusion occurring in January 1998 and modelled by using tilt and seismic data. The dyke was located on the upper north-western flank at 1 km a.s.l., with an opening of 75 cm (Bonaccorso and Patanè, 2001).

Starting from those models, several inversions using an L.S. approach have been performed, in order to refine the dyke parameters to fit GPS data. The best solution is a dyke 1.5 km wider and 7 km longer than the one proposed by Bonaccorso and Patanè (2001). Conversely, it is very similar to the one proposed by Puglisi and Bonforte (2004). However, looking at the residual between observed and calculated deformation, a good agreement is observed only on the summit and western areas of the volcano, whereas this source is not able to fit the ground deformation on the NE Rift area and on the eastern flank. For this reason, a further inversion was performed, starting from the results of the last one and introducing another two dislocations: the former is the "plane of sliding", just defined in the previous section, while the latter is a vertical dislocation source centred beneath the NE Rift area. In order to avoid inverting too many parameters, the parameters of the dyke were kept fixed to the results of previous inversions; furthermore the positions and dimensions of the "plane of sliding" were kept fixed, inverting only its dip- and strike-motion (its opening was forced to zero), while all the parameters of the "NE source" were completely inverted.

Finally, the combination of the three sources (Fig. 5c) produces GPS displacement vectors in good agreement with those observed. Looking at the differences between the observed and calculated deformation, a good fit was evident for the horizontal component, but a major residual affected some benchmarks, probably due to local effects.

The results of this inversion are summarized in Tables 2b and 3. The synthetic interferogram (in ascending mode), calculated for this period (Fig. 5d) shows a good agreement with the experimental data also (Fig. 4e): in fact, the misfit in the residual interferogram (Fig. 6e) is of the order of the estimated uncertainty in the InSAR data, with the exception of some residual fringes located along the NE Rift area and on the Valle del Bove area. Thus, a further refinement of the model obtained by inverting GPS data was not necessary.

Table 2
Parameters of the modelled sources for all the GPS comparisons considered in this work: a) 1993–1997; b) 1997–1998; c) 1998–2000; d) 1993–2000. Starting values used in the inversions are also reported. Coordinates are in UTM projection, zone 33N. Strike-slip is positive when sinistral

(a) 1993–1997

Parameters	Plane of sliding		Point source
	Starting v.	Final v.	
Longitude (km)	504.20	504.200	499.00
Latitude (km)	4172.03	4172.030	4178.10
Azimuth	N21°E	N21°E	
Depth (km)	1.4 b.s.l.	1.4 b.s.l.	5.7 b.s.l.
Length (km)	26.4	26.4	
Width (km)	12.34	12.34	
Dip	11.6°	11.6°	
Strike-slip (cm)	1.0	− 4.4±0.3	
Dip-slip (cm)	1.0	16.1±0.4	
Opening (cm)	0	0	
$P*a^3$ (Pa m^3)			2.26E+17

(b) 1997–1998

Parameters	Plane of sliding		Dyke		NE source	
	Starting v.	Final v.	Starting v.	Final v.	Starting v.	Final v.
Longitude (km)	504.20	504.20	498.53	500.70±0.02	501.00	502.30±0.02
Latitude (km)	4172.03	4172.03	4180.21	4178.50±0.02	4182.00	4182.80±0.01
Azimuth	N21°E	N21°E	N150°E	N158°E±0.5	N30°E	N163°W±0.5
Depth (km)	1.4 b.s.l.	1.4 b.s.l.	1.00	1.05±0.4 a.s.l.	1.50 a.s.l.	0.88±0.06 a.s.l.
Length (km)	26.4	26.4	6.40	8.76±0.05	4.0	6.0±0.05
Width (km)	12.34	12.34	1.90	5.5±0.06	2.0	3.40±0.05
Dip	11.6°	11.6°	60°	53.1°±0.7	89.9°	46°±1.0
Strike-slip (cm)	1.0	− 2.7±0.1	0	0	1.0	− 2.0°0.1
Dip-slip (cm)	1.0	1.3±0.1	0	0	1.0	− 1.0±0.1
Opening (cm)	0	0	18.0	13.7±0.2	1.0	10.1±0.1

(c) 1998–2000

Parameters	Plane of sliding		S source		NE source	
	Starting v.	Final v.	Starting v.	Final v.	Starting v.	Final v.
Longitude (km)	504.20	504.20	499.50	499.70±0.01	501.00	500.90±0.01
Latitude (km)	4172.03	4172.03	4175.10	4175.66±0.01	4182.00	4181.95±0.01
Azimuth	N21°E	N21°E	N5°E	N14°W±0.4	N30°E	N39°E±0.3
Depth (km)	1.4 b.s.l.	1.4 b.s.l.	1.50	0.4±0.01 a.s.l.	1.5 a.s.l.	1.8±0.01 a.s.l.
Length (km)	26.40	26.40	3.0	3.14±0.02	4.0	8.40±0.03
Width (km)	12.34	12.34	2.0	3.37±0.03	2.0	2.50±0.03
Dip	11.6°	11.6°	89.9°	49.3°±0.4	89.9°	39°±0.4
Strike-slip (cm)	1.0	− 3.6±0.2	1.0	3.2±0.2	1.0	− 2.07±0.1
Dip-slip (cm)	1.0	9.6±0.2	1.0	25.6±0.2	1.0	16.4±0.1
Opening (cm)	0	0	1.0	0	1.0	1.1±0.1

5.3. Inversion of the ground deformation measured from 1998 to 2000

From 1998 to 2000, the measured horizontal vectors seem to conflict with vertical deformations because the former suggest a general inflation of the volcano, while the latter generally subside, suggesting a deflation. A first attempt to invert this ground deformation pattern performed by using a Mogi (1958) source and the Simplex algorithm (Nunnari et al., 1995), failed because it found a source able only to fit the vertical movements. In order to justify the observed movements, a supervised inversion based on the Okada (1985) model and an L.S. approach was performed, by using as a "starting point" the same vertical dislocation plane used for the previous inversion (Table 2c). The solution converged to a

Table 2 (*continued*)

(d) 1993–2000

Parameters	Plane of sliding		Point source
	Starting v.	Final v.	
Longitude (km)	504.20	504.20	499.38
Latitude (km)	4172.03	4172.03	4178.92
Azimuth	N21°E	N21°E	
Depth (km)	1.4 b.s.l.	1.4 b.s.l.	6.5 b.s.l.
Length (km)	26.40	26.40	
Width (km)	12.34	12.34	

(d) 1993–2000

Parameters	Plane of sliding		Point source
	Starting v.	Final v.	
Dip	11.6°	11.6°	
Strike-slip (cm)	1.0	− 9.6 ± 0.2	
Dip-slip (cm)	1.0	26.1 ± 0.2	
Opening (cm)	0	0	
$P*a^3$ (Pa m^3)			4.00E + 17

shallow plane located beneath the NE Rift, striking NE-SW and dipping to SE. However, this source was unable to fit the ground deformation over the entire area, so a new inversion was performed by constraining the "NE source" to the values resulting from the previous inversion, and by adding a new vertical source beneath the South Rift area (Table 2c). Since the first runs, the inferred value of the opening of the S source was negative, then the opening was forced to zero. Finally, after several runs, the results of the inversion were able to fit the observed deformation on the summit area and on the western flank, though some misfit on the eastern sector of the volcano remains.

To reduce this misfit, a final inversion was performed by introducing the "plane of sliding" into the computation and constraining the "NE and S sources" to the values resulting from the previous inversion. Position and dimension of the "plane of sliding" were kept fixed, inverting only its dip- and strike-motion component (its opening was forced to zero).

Finally, the combination of these three sources was able to fit the ground deformation over the entire area. In Fig. 5e the location of the sources and the relevant expected horizontal displacement vectors are reported, while Table 2c summarizes the parameters of the modelled sources.

Looking at the differences between observed and calculated deformation, a good fit was evident for the horizontal component, while the vertical components are affected by major residuals. In particular, at the northern part of the N–S kinematic profile, the observed subsidence was 4 cm stronger than the calculated one. This is probably due to local tectonic effects.

Due to the low quality of the interferograms from this period (Fig. 4k, l), no synthetic data from models was calculated for the comparison and refinement of the GPS-based model.

5.4. Inversion of the ground deformation measured from 1993 to 2000

This time interval covers the entire period analysed in this work. In order to study it, we apply two different approaches. The former is not an inversion because we consider only the results of the models obtained in the previous sections; the latter consists of a true inversion with the same strategy adopted above.

The first approach was aimed at investigating the agreement between the displacements observed for 1993–2000 time interval and those expected by adding the effects of the different sources obtained in the previous inversions (1993–1997, 1997–1998 and 1998–2000). A general agreement was obtained for the horizontal components (white arrow-head in Fig. 5d), especially on the eastern flank, whereas the fit was not good for the vertical components (Table 3). Synthetic interferograms and residuals were calculated and are shown in Fig. 6f, g, h.

In the second approach, the inversion was attempted by maintaining the same structural framework (*i.e.* point source + plane of sliding source). The best solution is given by a pressure source located beneath the upper

Table 3
Code, UTM coordinates and height for each benchmark of Mt. Etna GPS network. Residual between observed and modelled components are also reported. For the 1993–2000 comparison, we also reported the residual between the observed components and those calculated by taking into account the effect of all the modelled sources

| Code	Long.	Lat.	Height	1993–1997			1997–1998			1998–2000			1993–2000 (total effects)			1993–2000 (modelling)		
				Δx	Δy	Δz	Δx	Δy	Δz	Δx	Δy	Δz	Δx	Δy	Δz	Δx	Δy	Δz
CAP	494784	4177299	1922				0.002	− 0.006	0.003	− 0.002	− 0.024	0.003						
CIS	500633	4175479	2682				− 0.006	− 0.001	− 0.003	− 0.002	0.011	0.034						
CIT	505241	4179808	1781	0.024	− 0.012	0.017	− 0.001	− 0.002	0.019	− 0.022	− 0.004	− 0.015	0.002	− 0.013	0.020	0.028	− 0.025	0.000
CRI	508250	4183202	1384	0.046	0.015	0.021	0.002	− 0.004	− 0.003	0.019	− 0.002	0.034	0.066	0.011	0.047	0.077	0.005	0.036
EPLU	498743	4179753	2964							− 0.006	− 0.006	− 0.009						
ESLN	497776	4171760	1774	0.008	0.018	0.019	− 0.002	− 0.009	0.031	0.010	0.001	− 0.008	0.005	0.022	0.094	0.000	− 0.006	− 0.016
GIA	515722	4174501	164				0.013	− 0.010	− 0.040	0.014	0.0	0.004						
L23	503092	4184205	1955	0.014	0.008	− 0.034	− 0.014	0.004	0.008	− 0.002	0.002	0.053	0.028	− 0.029	− 0.076	0.004	− 0.005	− 0.040
LAM	501013	4185857	1751	0.007	− 0.009	0.008	0.013	− 0.013	− 0.031	0.011	− 0.035	− 0.010	0.014	− 0.008	0.011	0.009	− 0.006	− 0.003
MIL	509308	4176052	921	0.030	− 0.027	− 0.039	− 0.010	0.002	0.017	0.006	0.004	− 0.004	0.024	− 0.051	− 0.068	− 0.015	− 0.042	− 0.027
MPL	501671	4162063	795				− 0.002	− 0.005	0.035	− 0.011	− 0.013	− 0.011						
NS01	502150	4183270	2134				− 0.008	− 0.008	0.045	0.003	0.009	− 0.031						
NS02	501282	4182457	2357				0.007	0.003	− 0.005	− 0.006	0.002	− 0.008						
NS03	500859	4181959	2456				0.009	− 0.009	0.010	0.003	0.003	− 0.027						
NS04	500616	4181603	2538				0.008	0.009	0.024	0.003	− 0.003	0.002						
NS05	500573	4181048	2656				0.019	0.002	− 0.002	0.012	0.003	− 0.007						
NS06	500461	4180450	2767				0.012	0.018	0.027	0.001	0.004	− 0.012						
NS07	500609	4180035	2849				− 0.006	0.004	0.037	0.0	0.010	− 0.025						
NS08	500187	4179784	2936				− 0.014	0.007	0.017	0.004	0.011	− 0.019						
NS09	499284	4179618	3006				0.002	0.013	− 0.027	0.0	− 0.005	0.019						
NS10	498946	4179351	3024				0.008	0.004	− 0.025	0.001	0.005	− 0.003						
NS11	498964	4178737	3140				− 0.002	0.011	− 0.019	− 0.023	0.006	− 0.035						
NS12	498849	4178351	3142				0.013	0.011	0.079									
NS13	498656	4177738	3051				0.004	0.001	0.030									
NS14	498999	4177187	3021				0.012	0.001	0.0									
NS15	499653	4176832	2984				− 0.001	− 0.007	0.006									
NS16	499984	4176345	2862				0.003	0.003	− 0.004	− 0.008	0.019	− 0.028						
NS17	500041	4176114	2798				− 0.005	0.001	0.001	0.007	0.015	− 0.005						
NS18	500386	4175473	2689				− 0.016	0.005	0.020	0.014	0.019	− 0.026						
NS19	499959	4174704	2553				0.0	0.010	0.004	− 0.008	0.004	− 0.010						
NS20	499759	4174442	2476				0.002	0.010	0.004	− 0.007	0.005	− 0.025						
NS21	499579	4173308	2175				− 0.008	0.012	0.029	− 0.003	− 0.013	− 0.034						
NS22	500009	4172669	1973				− 0.004	0.013	0.004	− 0.009	− 0.012	0.014						
NUN	495830	4179543	1830	0.018	− 0.019	− 0.027	0.027	0.0	− 0.014	− 0.008	− 0.024	− 0.014	0.010	− 0.011	− 0.004	0.022	− 0.021	− 0.056
OBS	501342	4180162	2819	0.005	− 0.019	− 0.039	− 0.010	0.008	0.039	− 0.006	0.007	− 0.023	0.007	− 0.003	− 0.028	0.021	− 0.018	− 0.076
OSV	501476	4179830	2867	0.035	− 0.033	− 0.070	− 0.011	0.001	0.048	0.005	0.015	− 0.041	0.025	− 0.034	− 0.086	0.049	− 0.042	− 0.098
PAR	497201	4170245	1552				− 0.007	− 0.006	0.052	0.011	− 0.015	− 0.067						
PDG	488867	4177328	1214				− 0.003	− 0.009	0.014	− 0.009	− 0.006	0.007						
PLU	499117	4179835	2970	0.014	− 0.047	0.011	0.018	0.014	− 0.027	− 0.006	− 0.002	0.001	0.024	− 0.045	0.035	0.007	0.080	0.048
STP	505486	4172033	1328	− 0.014	− 0.002	0.037	− 0.001	− 0.008	0.019	− 0.008	− 0.002	0.017	− 0.021	− 0.009	0.066	− 0.024	− 0.007	0.051
TDF	500084	4176702	2966				− 0.002	0.003	− 0.006									
TUR	490507	4174001	1326	− 0.004	−0.020	0.016	− 0.014	0.007	0.034	− 0.009	− 0.018	− 0.014	− 0.015	− 0.038	0.004	− 0.049	− 0.036	0.003
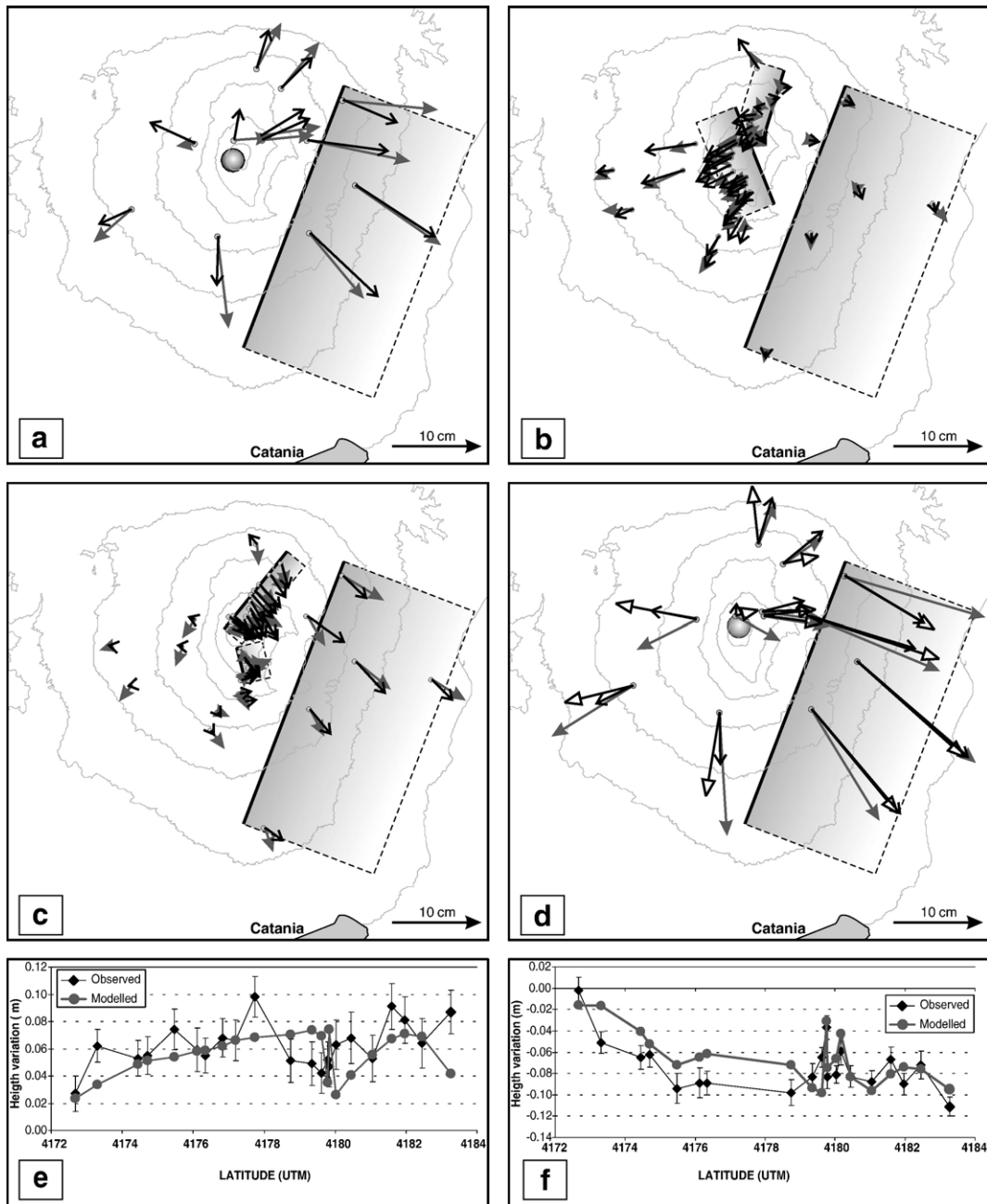
Fig. 5. Comparison between observed (grey arrows) and expected (black arrows) horizontal displacements relevant to the following periods: (a) 1993–1997; (b) 1997–1998; (c) 1998–2000; (d) 1993–2000. Modelled sources are also reported. For the 1993–2000 time intervals, we also reported the expected horizontal displacements (white arrow-heads) calculated by taking into account the effect of all modelled sources (Table 2a–c). The height variations observed along the N–S kinematic profile during the 1997–1998 (e) and 1998–2000 (f) comparisons are reported, together with the vertical deformation expected from the models.

western flank of the volcano at a depth of about 6.5 km, with a strength of $4.0 * 10^{17}$ Pa m^3, while the "plane of sliding" showed a strike/dip ratio of 0.37, in between those inferred from the 1993–1997 (0.27) and 1998–2000 (0.38) inversions (Tables 2d and 3). The predicted vector

displacements, the synthetic and residual interferograms are reported respectively in Figs. 5d and 6i, j, k.

Looking at the synthetic interferograms relevant to the results of the two different approaches adopted for this time interval (Fig. 6f, i), the main differences
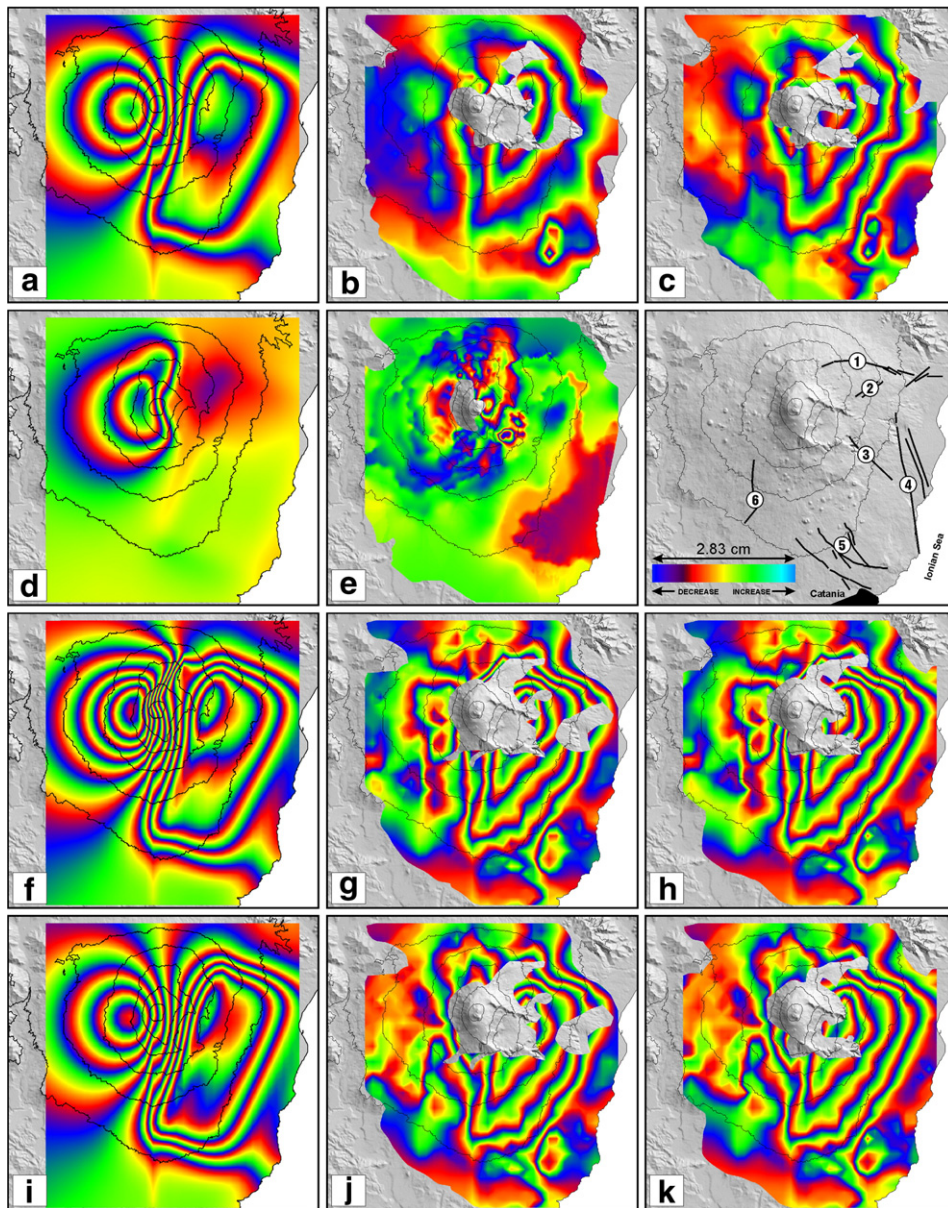
Fig. 6. Predicted and residual (difference between predicted and observed one) ascending interferograms. (a) Synthetic interferograms for the 1993–1997 time interval; (b) residual interferogram calculated with respect to the 4a observed one; (c) residual interferogram calculated for the 4c observed one; (d) synthetic interferograms for the 1997–1998 time interval; (e) residual interferogram calculated for the 4e observed one; (f) synthetic interferograms for the 1993–2000 time interval calculated from the sum of the modelled sources from Table 2a–c; (g) residual interferogram calculated for the 4m observed one; (h) residual interferogram calculated for the 4n observed one; (i) synthetic interferograms for the 1993–2000 time interval derived from the modelled sources (Table 2d); (j) residual interferogram calculated for the 4m observed one; (k) residual interferogram calculated for the 4n observed one. Each fringe represents a change in phase corresponding to 2.83 cm of LOS. A sketch map of Mt. Etna showing the main tectonic features (see text in Section 4 and Fig. 1 for details) is also reported.

between the two interferograms are the higher number of fringes and the complex deformation pattern along the NE Rift zone observed in Fig. 6f with respect to Fig. 6i. The experimental data (Fig. 4m, n) better agree with Fig. 6i because of the same shape and number of fringes. Unfortunately, the lack of coherency along the NE Rift

zone, observed in the experimental data (Fig. 4m, n) hinders the validation of the local pattern expected from the synthetic data (Fig. 6j, k).

In general, the models we obtained fit the data well. However, we observe some non-negligible effects on residual interferograms (Fig. 6). The models

indeed cannot sufficiently explain the ground deformation on the eastern flank of the volcano. Possible origins of the misfits are: (i) atmospheric noise; (ii) oversimplification of the models and (iii) tectonic activity of faults.

As mentioned in Section 4, atmospheric noise can account about 1.5–2 fringes from the base of the volcano up to the summit. Thus, residual interferograms showing less than 2 fringes can be considered acceptable.

We assumed the simple Okada formalism (1982) to model the sliding plane of the eastern flank. It has been successfully applied at Hawaii (Owen et al., 2000; Cervelli et al., 2002) to model the deformation pattern in similar conditions. However, it is able to perform a first-order modelling of the observed deformation pattern, because the assumption of this model (homogeneous, isotropic and elastic half-space with flat surface) could represent an oversimplification of actual conditions.

Regarding the tectonic activity, several faults dissect mainly the eastern sector of the volcano (Fig. 1). They have been active during the investigated period (Azzaro et al., 2000; http://www.ct.ingv.it/Sismologia/macro/default.htm) as detected by InSAR (Fig. 4). The deformation pattern caused by those structures cannot be produced in our models, because simple structures cannot take into account such a complex framework.

6. Data interpretation and discussion

The ground deformation sources inferred in the previous sections are now discussed in order to depict a coherent evolution of the ground deformation pattern from 1993 to 2000, by considering the volcanological and geophysical knowledge. The dataset allows us to analyse both long- and short-time intervals. In the following, after discussing the long-time periods, mainly on the deep source, the shallow sources are then considered by examining short periods.

6.1. Deep sources

The inversions of GPS data for long-time periods (1993–1997 and 1993–2000) indicate pressure sources beneath the upper western flank of the volcano, at 5.7–6.5 km b.s.l. These pressure sources could be interpreted as a sort of "average" of the sources that were active throughout the seven-year period due to the uprising magma, which probably fed the shallow intrusions and eruptions occurring from 1995 to 2000, similarly to what was discussed by Puglisi and Bonforte (2004) between 1993 and 1998. This

interpretation is also consistent with the results of Houlié et al. (2006), who modelled the velocities from 1994 to 1999 measured on the same GPS network but using a different processing approach and software. They obtained a Mogi-type source located at depth of 6.5 ± 1 km b.s.l., whose horizontal position is very close to that obtained in the present paper. One difference between this and the Houlié et al. (2006) paper concerns the "intensity" of these sources. Assuming a rigidity of 30 GPa, the strength of the Houlié source is $2.6 * 10^{17}$ Pa m^3, *i.e.* about 1.0–1.6 times smaller than that obtained in this paper. However, considering the large approximations in elastic parameters and the significant differences in the nature of the datasets this discrepancy is of secondary order.

The first evidence of an active ground deformation source beneath the upper western flank of the volcano was obtained by Nunnari and Puglisi (1994) by using GPS data collected in 1990–1991. Subsequently, ground deformation sources beneath the upper western flank of Mt. Etna have been invoked (Bonaccorso, 1996; Puglisi et al., 2001) and the differences in shape and depth of these sources might be considered negligible from the volcanological point of view (Puglisi et al., 2001) because they could be related either to the uncertainty in the measurement and/or inversion procedures, or to the actual changes in the location of the centre of pressure along a planar path of the rising magma. In summary, looking at the depths of the pressure sources previously proposed, ranging from 3 to 9 km b.s.l. (Puglisi and Bonforte, 2004), and the depths resulting in the present study, we suggest that at least a part of the feeding system of Mt. Etna is centred on the upper western part of the volcano, located in a volume whose projection on the surface is relatively small (few km^2). This conclusion is in agreement with the crustal structure of Mt. Etna recently revealed by seismic tomography (Chiarabba et al., 2000; Laigle et al., 2000; Patanè et al., 2002).

6.2. Shallow sources

At shallow depths (1–2 km a.s.l), the modelled sources highlight some particular features. The combination of the structures inferred from the 1997–1998 and 1998–2000 inversions forms locally two graben-like structures (Fig. 7); the former is located beneath the NE Rift area and is characterised by two planes with low dip angles and a NE-SW trend; the latter is located beneath the South Rift area showing a NNW-SSE trend, and characterised by two planes with low dip angles too. However, the similarity with a graben structure is only
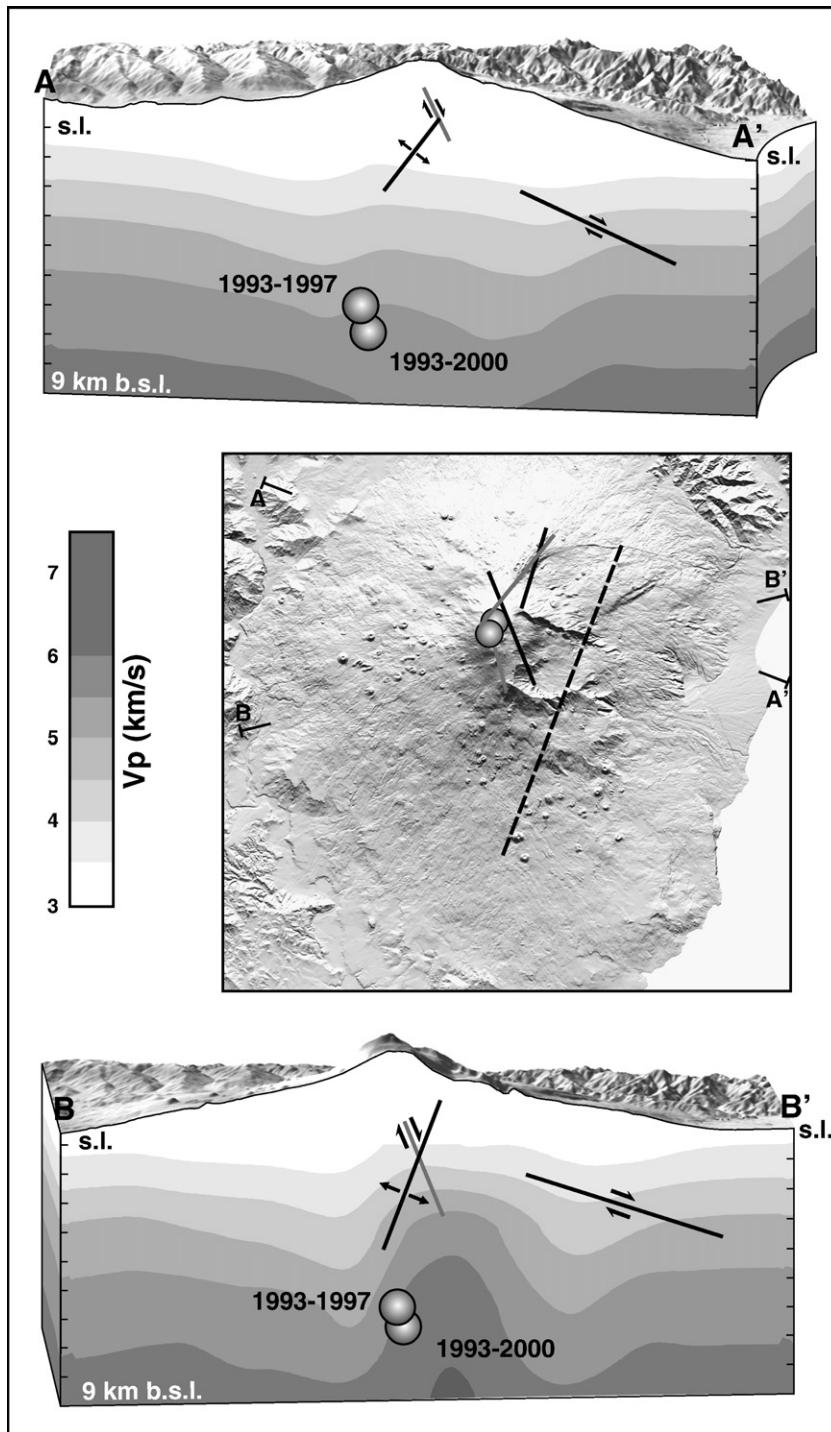
Fig. 7. Schematic cross sections (A–A', B–B') showing the geometrical relationships between the different planar structures modelled in this work for the 1997–1998 (black) and 1998–2000 (dark grey) time intervals. The pressure sources detected for the 1993–1997 and 1993–2000 are also reported. Vertical exaggeration is 2. V_P values resulting from the Chiarabba et al. (2000) tomography are also reported. Velocity contours are every 0.5 km/s.

geometric because the kinematics of these structures did not conform to the typical opening behaviour of graben features along rift zones. This similarity is indeed only

apparent because the two active sides of each "graben-like" structure show different behaviours at different times.

For the time interval 1997–1998, encompassing the shallow intrusive episode, the inversion of GPS data inferred two opening dislocation sources, both west-dipping and located beneath the summit area. The southern one is 1.5 km wider and 7 km longer than the dyke proposed by Bonaccorso and Patanè (2001), but very similar to the one proposed by Puglisi and Bonforte (2004). However, all the dykes proposed for this intrusive episode (i. e. that obtained in this paper and those previously published) show the same NNW-SSE trend, the same dip and a very similar dip angle, suggesting that the different dimensions are due either to the different time intervals considered (namely, shorter for Bonaccorso and Patanè, 2001 with respect to the one considered in this paper) or dataset (namely, only GPS for Puglisi and Bonforte, 2004 and GPS and InSAR for this paper). The integrated GPS and InSAR approach used in this paper allows us to infer the presence and kinematics of the NE source, whose movement is dominated by the opening component. As the shallower crust present in the NE Rift zone is highly fractured by faults and joints, due to several eruptive events occurring in this area, we could assume that part of the magma migrated toward the Rift zone, probably taking advantage of the pre-existent "voids". In light of this, we can assess that the weak NE Rift showed a passive behaviour as a response to the intrusive episode occurring beneath the upper southern flank in this period.

In the following time interval (1998–2000), the GPS data inversion inferred an east-dipping structure beneath the NE Rift showing a slip dominated by a normal dip-slip component and a minor right strike-slip. A high value of a normal dip-slip component associated with a minor left strike-slip component is also exhibited by the South source detected for the same period. The strike-slip obtained by using the GPS and InSAR data are not consistent with the known structural framework of Mt. Etna where, left strike-slip is expected in the NE Rift zone and right strike-slip in the South Rift zone. In our opinion, those anomalies could be due either to the deflation affecting the upper part of the volcano and/or to the weak behaviour of the two rift zones (Rasà et al., 1996).

6.3. Dynamic of the eastern flank

At the scale of the volcano, the inferred NNW-SSE and NE-SW trends represent the most frequent orientation of the magmatic intrusions and tensile dislocations at Mt. Etna. These two primary structural trends can be recognizable both in the regional context and in the volcanic area (Fig. 1). The former can be traced southwards along the NNW-SSE-oriented Malta Escarpment (Monaco et al., 1997), while the latter can be traced northwards along the NE-SW striking Messina fault system to the inner side of the Calabrian orogenic arc. Etnean seismicity often takes place in swarms and/or clusters along the NNW-SSE and NE-SW structural trends (Bonaccorso, 1996; Gresta et al., 1998; Patanè and Privitera, 2001). Their activation in the central and western parts of the volcano is linked to relevant changes both in seismic and volcanic activity (Bonaccorso and Patanè, 2001). The two fault systems play a key role also in the dynamics of the volcano's eastern flank. The eastern sector is affected by a constant eastward to south-eastward motion, detected by both GPS and InSAR data. Several authors have already suggested that the eastern flank of Mt. Etna is moving toward the sea, by carrying out studies based on geological, structural, and geomorphologic data (Borgia et al., 1992; Rasà et al., 1996). However, since those studies lack any direct measurement of the current movements, several points of this hypothesis are still controversial, in particular those related to the source and location of the boundary of moving blocks. In this paper, the analytical model inferred a plane dipping about 12°ESE, located beneath the eastern flank of the volcano at a depth of 1.4 km b.s.l. This plane, very similar to that proposed by Bonforte and Puglisi (2003), drives the south-eastward motion of a sector bounded to the north by the Pernicana fault, to the west by the NE Rift and the South Rift, and to the south by the Mascalucia–Tremestieri–Trecastagni fault system. This structural framework leads us to interpret the eastern sector as a mega-block bounded by shallow trans-tensional faults, which progressively flatten at depth (1–2 km b.s.l.) into a main sliding "zone" which is described by the "plane of sliding" in the analytical model.

This sliding zone is located just above the boundary between two crustal volumes characterised by different elastic properties, as detected by recent seismic tomographies (Chiarabba et al., 2000; Laigle et al., 2000; Patanè et al., 2002). The shallowest shows V_P velocities typical of a heterogeneous upper crust (Chiarabba et al., 2000). The lowest, conversely, is a high-V_P body which is interpreted as high-density cumulates, fractionated during repeated intrusions (Chiarabba et al., 2000; Laigle et al., 2000; Patanè et al., 2002) or as fossil magma chambers of previous volcanoes, that migrated toward the SE together with their effusive and sedimentary cover (Laigle et al., 2000).

Our results confirm the importance of the sliding zone in the dynamics of Mt. Etna's eastern flank.

Indeed, the distribution patterns of the residuals between observed and modelled deformations show the high mobility of the eastern flank with respect to the remaining part of the volcano. If we consider volcanic sources alone (dykes or pressure sources), an eastward rotation of the residual vectors and strong vertical misfits are always visible on the eastern flank. This confirms that the deformations of this flank are driven by both its downslope movement and volcanic sources. Furthermore, looking at the strike-slip/dip-slip ratio (and consequently at the rake value) for each time interval, we observed a steady value of this ratio (ranging from 0.27 to 0.38) for 1993–1997, 1998–2000, and 1993–2000 time intervals, and an anomalous value of the ratio (2.1) for the 1997–1998 time interval. In light of the intrusive episode in January 1998, our results suggest that the rake of the movement on the sliding plane is strongly sensitive to the volcanic activity.

6.4. Dynamic of Mt. Etna from 1993 to 2000

GPS data and InSAR data, between 1993 and 1997, indicate a re-pressurization of Mt. Etna's plumbing system, which triggered most of the seismicity and induced the dilatation of the volcano, producing a series of eruptions at the summit of the volcano from 1995. A deep intrusion was detected by InSAR, between March and May 1997, on the western flank of the volcano (cfr. points 3a and 3b in Section 4). This concurs with the deep source (9 km b.s.l.) proposed by Puglisi and Bonforte (2004) detected by GPS data inversions from 1996 to 1997. In the following months, this intrusion seems to rise (cfr. point 3c in Section 4) leading to a seismic swarm occurring between January 9th and 14th 1998 in the western sector (Bonaccorso and Patanè, 2001). This shallow intrusion is confirmed by GPS data also, by comparing the 1997 and the 1998 surveys. After this event, beside the mild persistent activity at SEC, the summit craters showed erratic or no activity for about three months. In the summer of 1998, an increase in eruptive activity, characterised both by strombolian and effusive activities, was observed until the end of 2000. This vigorous summit activity was accompanied by a deflation confined to the upper part of the volcano as detected from GPS and InSAR data for the 1998–2000 time interval.

7. Concluding remarks

Mt. Etna is one of the most studied volcanoes in the world using InSAR data (*i.e.* Massonnet et al., 1995;

Lanari et al., 1998; Lundgren et al., 2003). In this work, ground deformation at Mt. Etna has been studied using both InSAR and GPS data. Both techniques highlight some features of the volcano behaviour from 1993 to 2000. By looking at different ground deformation patterns during different time windows we can draw the following conclusions:

1. InSAR and GPS data show that the magma started to fill the plumbing system of the volcano in 1993. However, only in 1995 did summit eruptions begin. InSAR detected a deep intrusion on the western flank of the volcano, between March and May 1997. In the following months this intrusion rose, leading to a seismic swarm in January 1998. From 1998 to 2000, a general deflation affected the upper part of the volcano.
2. The inversions for long-time periods (1993–1997 and 1993–2000) support the idea of pressure sources beneath the upper western flank of the volcano, at 5.7–6.5 km b.s.l. Considering also previous models, we suggest that a part of the feeding system of Mt. Etna is vertically elongated, and located in a volume whose projection on the surface is relatively small (few km^2) and centred on the upper western part of the volcano.
3. The inversion for short-time periods (1997–1998 and 1998–2000) highlighted that the NNW-SSE and NE-SW are the most frequent orientations for shallow magmatic intrusions and tensile dislocations. Furthermore, the combination of the structures inferred from these inversions forms locally two graben-like structures. However, these structures are similar to a graben only from a geometrical point of view because their kinematics strongly depends on the response of the weak shallower crust in the rift zone to the volcanic activity.
4. Both GPS and InSAR data showed a continuous eastward to south-eastward motion of part of the eastern sector of the volcano. They confirm the lateral boundaries of the sliding sector. The bottom has been modelled by a plane dipping about 12°ESE, located beneath the eastern flank of the volcano at a depth of 1.4 km b.s.l. The analysis of the strike-slip/dip-slip ratio for each time interval considered in this work, shows that the movement on this plane is strongly sensitive to the volcanic activity.

References

Azzaro, R., 1999. Earthquake surface faulting at Mt. Etna volcano (Sicily) and implications for active tectonics. J. Geodyn. 28, 193–213.

Azzaro, R., Barbano, M.S., Antichi, B., Rigano, R., 2000. Macroseismic catalogue of Mt. Etna earthquake from 1832 to 1998. Acta Vulcanol. 12, 3–36.

Azzaro, R., Mattia, M., Puglisi, G., 2001. Dynamics of fault creep and kinematics of the eastern segment of the Pernicana fault (Mt. Etna, Sicily) derived from geodetic observations and their tectonic significance. Tectonophysics 333, 401–415.

Beauducel, F., Briole, P., Froger, J.L., 2000. Volcano-wide fringes in ERS synthetic aperture radar interferograms of Etna (1992–1998): deformation or tropospheric effect? J. Geophys. Res. 105, 16391–16402.

Beutler, G., Gurtner, W., Rotacher, M., Wild, U., Frei, E., 1990. Relative static positioning with the Global Positioning System: basic technical considerations. Global Positioning System: An Overview. IAG Symposium. Springer-Verlag, Berlin, pp. 1–23.

Bonaccorso, A., 1996. Dynamic inversion of ground deformation data for modeling volcanic sources (Etna 1991–93). Geophys. Res. Lett. 23, 451–454.

Bonaccorso, A., Patanè, D., 2001. Shear response to an intrusive episode at Mt. Etna volcano (January 1998) inferred through seismic and tilt data. Tectonophysics 334, 61–75.

Bonforte, A., Puglisi, G., 2003. Magma uprising and flank dynamics on Mount Etna volcano studied using GPS data (1994–1995). J. Geophys. Res. 108, 2153–2162.

Bonforte, A., Ferretti, A., Prati, C., Puglisi, G., Rocca, F., 2001. Calibration of atmospheric effects on SAR interferograms by GPS and local atmosphere models: first results. J. Atmos. Sol.-Terr. Phys. 63, 1343–1357.

Borgia, A., Ferrari, L., Pasquarè, G., 1992. Importance of gravitational spreading in the tectonic and volcanic evolution of Mount Etna. Nature 357, 231–235.

Borgia, A., Lanari, R., Sansosti, E., Tesauro, M., Berardino, P., Fornaro, G., Neri, M., Murray, J.B., 2000. Actively growing anticlines beneath Catania from distal motion of Mount Etna's decollement measured by SAR interferometry and GPS. Geophys. Res. Lett. 27, 3409–3412.

Briole, P., Gaulon, R., Nunnari, G., Puglisi, G., Ruegg, J.C., 1992. Measurements of ground movement on Mount Etna, Sicily: a systematic plan to record different temporal and spatial components of ground movement associated with active volcanism. In: Gasparini, P., Scarpa, R., Aki, K. (Eds.), IAVCEI Proceedings in Volcanology. Springer-Verlag, Berlin, pp. 120–129.

Briole, P., Massonnet, D., Delacourt, C., 1997. Post-eruptive deformation associated with the 1986–97 and 1989 lava flows of Etna detected by radar interferometry. Geophys. Res. Lett. 24, 37–40.

Cervelli, P., Segall, P., Johnson, K., lisowski, M., Miklius, A., 2002. Sudden aseismic fault slip on the south flank of Kilawea volcano. Nature 415, 1014–1018.

Chiarabba, C., Amato, A., Boschi, E., Barberi, F., 2000. Recent seismicity and tomographic modeling of the Mount Etna plumbing system. J. Geophys. Res. 105, 10923–10938.

Coltelli, M., Pompilio, M., Del Carlo, P., Calvari, S., Pannucci, S., Scribano, V., 1998. Mt. Etna: the eruptive activity (1993–1995). Acta Vulcanol. 10, 141–148.

Delacourt, C., Briole, P., Achache, J., 1998. Tropospheric corrections of SAR interferograms with strong topography. Application to Etna. Geophys. Res. Lett. 25, 2849–2852.

Froger, J.L., Merle, O., Briole, P., 2001. Active spreading and regional extension at Mount Etna imaged by SAR interferometry. Earth Planet. Sci. Lett. 148, 245–258.

Gresta, S., Bella, D., Musumeci, C., Carveni, P., 1997. Some efforts on active faulting processes (earthquakes and aseismic creep) acting on the eastern flank of Mt. Etna (Sicily). Acta Vulcanol. 9, 101–108.

Gresta, S., Peruzza, L., Slejko, D., Distefano, G., 1998. Inferences on the main volcano-tectonic structures at Mt. Etna (Sicily) from a probabilistic seismological approach. J. Seismol. 2, 105–116.

Houlié, N., Briole, P., Bonforte, A., Puglisi, G., 2006. Large scale ground deformation of Etna observed by GPS between 1994 and 2001. Geophys. Res. Lett. 33. doi:10.1029/2005GL024414.

INGV staff, 2001. Multidisciplinary approach yields insight into Mt. Etna eruption. EOS 82, 653–656.

Laigle, M., Hirn, A., Sapin, M., Lépine, J.C., Diaz, J., Gallart, J., Nicolich, R., 2000. Mount Etna dense array local earthquake P and S tomography and implications for volcanic plumbing. J. Geophys. Res. 105, 21633–21646.

Lanari, R., Lundgren, P., Sansosti, E., 1998. Dynamic deformation of Etna volcano observed by satellite radar interferometry. Geophys. Res. Lett. 25, 1541–1544.

Lentini, F., 1982. The geology of the Mt. Etna basement. Mem. Soc. Geol. Ital. 23, 7–26.

Lo Giudice, E., Patanè, G., Rasà, R., Romano, R., 1982. The structural framework of Mount Etna. Mem. Soc. Geol. Ital. 23, 125–158.

Lundgren, P., Berardino, P., Coltelli, M., Fornaro, G., Lanari, R., Puglisi, G., Sansosti, E., Tesauro, M., 2003. Coupled magma chamber inflation and sector collapse slip observed with SAR interferometry on Mt. Etna volcano. J. Geophys. Res. 108, 2247–2261.

Lundgren, P., Casu, F., Manzo, M., Pepe, A., Berardino, P., Sansosti, E., Lanari, R., 2004. Gravity and magma induced spreading of Mount Etna volcano revealed by satellite radar interferometry. Geophys. Res. Lett. 31. doi:10.1029/2003GL018736.

Massonnet, D., Feigl, K., 1998. Radar interferometry and its application to changes in the Earth's surface. Rev. Geophys. 36, 441–500.

Massonnet, D., Briole, P., Arnaud, A., 1995. Deflation of Mount Etna monitored by spaceborne radar interferometry. Nature 375, 567–570.

McGuire, W.J., Pullen, A.D., 1989. Location and orientation of eruptive fissures and feeder-dykes at Mount Etna; influence of gravitational and regional tectonic stress regimes. J. Volcanol. Geotherm. Res. 38, 325–344.

McGuire, W.J., Moss, J.L., Saunders, S.J., Stewart, I.S., 1996. Dyke-induced rifting and edifice instability at Mount Etna. In: Gravestock, P.J., McGuire, W.J. (Eds.), Etna: fifteen years on. Cheltenham and Gloucester Spec. Publ., pp. 20–24.

McTigue, D.F., 1987. Elastic stress and deformation near a finite spherical magma body: resolution of the point source paradox. J. Geophys. Res. 92, 12931–12940.

Mogi, K., 1958. Relation between the eruptions of various volcanoes and the deformations of the ground surface around them. Bull. Earthq. Res. Inst. Univ. Tokyo 36, 99–134.

Monaco, C., Tapponnier, P., Tortorici, L., Gillot, P.Y., 1997. Late Quaternary slip-rate on the Acireale-Piedimonte normal faults and tectonic origin of Mount Etna. Earth Planet. Sci. Lett. 147, 125–139.

Nunnari, G., Puglisi, G., 1994. Ground deformation studies during the 1991–1993 Etna eruption using GPS data. Acta Vulcanol. 4, 101–107.

Nunnari, G., Puglisi, G., Maugeri, S.R., 1995. An optimisation approach for the inversion of ground deformation data. Volcanic Monitoring. Cahiers de Centre Européen de Geodynamique et de Seismologie, Walferdange, Luxembourg, pp. 259–277.

Okada, Y., 1985. Surface deformation due to shear and tensile fault in half-space. Bull. Seismol. Soc. Am. 75, 1135–1154.

Owen, S., Segall, P., Lisowski, M., Miklius, A., Delinger, R., Sako, M., 2000. Rapid deformation of Kilawea Volcano: Global Positioning System measurements between 1990 and 1996. J. Geophys. Res. 105, 18983–18998.

Palano, M., 2003. InSar techniques in structural geology: some applications to Mt. Etna volcano. University of Catania, Italy, 145 pp.

Palano, M., Puglisi, G., Gresta, S., 2007. Ground deformation at Mt. Etna: a joint interpretation of GPS and InSAR data from 1993 to 2000. Boll. Geofis. Teor. Appl. 48, 81–98.

Patanè, D., Privitera, E., 2001. Seismicity related to 1989 and 1991–93 Mt. Etna (Italy) eruptions: kinematic constraints by fault solution analysis. J. Volcanol. Geotherm. Res. 109, 77–98.

Patanè, D., Chiarabba, C., Cocina, O., De Gori, P., Moretti, M., Boschi, E., 2002. Tomographic images and 3D earthquake locations of the seismic swarm preceding the 2001 Mt. Etna eruption: evidence for a dyke intrusion. Geophys. Res. Lett. 29. doi:10.1029/2001GL014391.

Puglisi, G., Bonforte, A., 2004. Dynamics of Mount Etna volcano inferred from static and kinematic GPS measurements. J. Geophys. Res. 109. doi:10.1029/2003JB002878.

Puglisi, G., Bonforte, A., Maugeri, S.R., 2001. Ground deformation patterns on Mt. Etna, between 1992 and 1994, inferred from GPS data. Bull. Volcanol. 62, 371–384.

Puglisi, G., Guglielmino, F., 1995. Sperimentazione del GPS semi-cinematico per applicazioni geodinamiche. Proc. 13th Ann. Conf. GNGTS, Rome, October 23–25, pp. 361–372.

Rasà, R., Azzaro, R., Leonardi, O., 1996. Aseismic creep on faults and flank instability at Mt. Etna volcano. In: McGuire, W.J., Jones, A.P., Neuberg, J. (Eds.), Volcano instability on the Earth and other planets. Geol. Soc. London Spec. Publ., vol. 110, pp. 179–192.

Rust, D., Neri, M., 1996. The boundaries of large-scale collapse on the flanks of Mount Etna, Sicily. In: McGuire, W.J., Jones, A.P., Neuberg, J. (Eds.), Volcano instability on the Earth and other planets. Geol. Soc. London Spec. Publ., vol. 110, pp. 193–208.

Trasatti, E., Giunchi, C., Bonafede, M., 2003. Effects of topography and rheological layering on ground deformation in volcanic regions. J. Volcanol. Geotherm. Res. 122, 89–110.

Williams, C.A., Wadge, G., 2000. An accurate and efficient method for including the effects of topography in three-dimensional elastic models of ground deformation with applications to radar interferometry. J. Geophys. Res. 105, 8103–8120.